

# Prototyping Flexible Supercapacitors

## Produced with Biohydrogel

**Maricruz G. Saborío,<sup>1,2</sup> Šejla Zukić,<sup>1</sup> Sonia Lanzalaco,<sup>1,2</sup> Jordi Casanovas,<sup>3</sup> Jordi Puiggali,<sup>1,2</sup> Francesc Estrany,<sup>1,2,\*</sup> and Carlos Alemán<sup>1,2,\*</sup>**

<sup>1</sup> *Departament d'Enginyeria Química, EEBE, Universitat Politècnica de Catalunya, C/ Eduard Maristany 10-14, Ed. I2, 08019 Barcelona, Spain*

<sup>2</sup> *Barcelona Research Center for Multiscale Science and Engineering, Universitat Politècnica de Catalunya, Eduard Maristany 10-14, 08019 Barcelona, Spain*

<sup>3</sup> *Departament de Química, Escola Politècnica Superior, Universitat de Lleida, c/Jaume II no. 69, Lleida E-25001, Spain*

\* Corresponding authors: [francesc.estrany@upc.edu](mailto:francesc.estrany@upc.edu) and [carlos.aleman@upc.edu](mailto:carlos.aleman@upc.edu)

## **ABSTRACT**

Flexible symmetric supercapacitor prototypes composed of electrodes that were prepared by polymerizing poly(hydroxymethyl-3,4-ethylenedioxythiophene) inside a poly- $\gamma$ -glutamic acid ( $\gamma$ PGA) biohydrogel matrix, previously loaded with microparticles of poly(3,4-ethylenedioxythiophene) (PEDOT) and alumina ( $\text{Al}_2\text{O}_3$ ), have been fabricated and characterized. Prototypes have been assembled in a totally solid, compact and lightweight configuration, where the supporting electrolytic medium is a  $\gamma$ PGA prepared in presence of  $\text{NaHCO}_3$ . After characterization of the elements involved in the prototypes, their dimensions (*i.e.* lengths of the electrode and the solid electrolyte) have been optimized to obtain the highest specific capacitance. The electrochemical performances of the prototypes have been investigated by cyclic voltammetry, charge-discharge galvanostatic cycles and electrochemical impedance spectroscopy. After 2000 charge-discharge cycles (*i.e.* 60.000 s of continuous operation), the loss of specific capacitance is of only 8%, revealing an excellent stability. Results are very promising for the development of compact, flexible, lightweight and biocompatible supercapacitors to be employed like energy-autonomous electronic devices.

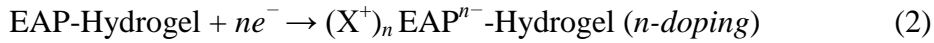
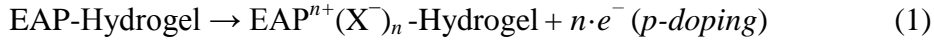
## INTRODUCTION

New energy storage devices based on electroactive polymers (EAPs) and produced using novel accessible techniques are currently emerging as a response to recent requirements of sustainable, non-hazardous, lightweight, flexible, and compact (nano and microscale) electronic apparatus. Materials used for such energy applications can be applied in different fields, which include wearable technologies,<sup>1</sup> flexible mobile phone,<sup>2</sup> conductive adhesives,<sup>3</sup> active electrodes for capacitors or supercapacitors<sup>3-6</sup> and hybrid lithium-ion batteries.<sup>7</sup> Additionally, due to their excellent biocompatibility, some of these electroactive materials<sup>8</sup> also find applications in biomedicine, for example as biosensors,<sup>9-11</sup> transducers,<sup>12</sup> regenerative tissues,<sup>13-15</sup> drug release devices,<sup>10,11,16,17</sup> neural and recording devices.<sup>18-20</sup>

Nowadays, supercapacitors based on flexible materials, like electroactive hydrogels that fundamentally involve co-networks of EAPs and hydrated hydrogels, constitute an appealing research subject of many investigations.<sup>19-21</sup> EAP-hydrogel composites have lots of benefits, as for example, unique energy storage capacity, which are reached through their large surface area (40-100 m<sup>2</sup>/g), structural adaptability, and 3D hierarchical porosity.<sup>4</sup> These materials are characterized by rapid and short charge transport pathways, obtained as a combination of porous hydrogel matrix, low characteristic interfacial impedance and intrinsic properties of the EAPs.<sup>5,22</sup>

Some EAPs used for the preparation of electroactive hydrogels are polyacetylene, poly(*p*-phenylene), polyaniline, polypyrrole, poly(phenylenevinylene), poly(ethyleneimine), and polythiophene.<sup>11,13,22</sup> These materials exhibit high electrical conductivity (from a few to 1000 S cm<sup>-1</sup> in the doped state) and low band-gap (1–3 eV) as fundamental properties.<sup>7</sup> These inherent and distinctive peculiarities are due to the combination of a characteristic electronic structure (*i.e.* EAPs show a conjugated

structure with alternating single and double bonds) and the doping process (*i.e.* chemical and electrochemical reactions to form polarons and bipolarons that act as charge carriers).<sup>4,13</sup> Thus, EAPs can be p-doped or n-doped through oxidation (anions as counter-ions) or reduction (cations as counter-ions), respectively. In the case of EAP-hydrogel composites, the general equations for these two charging processes are:<sup>7</sup>



where  $\text{X}^-$  and  $\text{X}^+$  refer to the counter-anion and counter-cation, respectively.

The preparation of electroactive hydrogels has been achieved using different procedures, as for example formation of cross-links among the own EAP chains, chemical coupling of EAP chains to a dielectric hydrogel matrix, printing the EAP on the hydrogel substrate and polymerization of the whole composite in a one-step process using the same compound as gelator and dopant.<sup>22-26</sup>

Currently, one of the most employed EAPs is the poly(3,4-ethylenedioxythiophene) (PEDOT), which can be easily obtained by anodic polymerization in different conditions. In a pioneering work, Sasaki *et al.*<sup>14</sup> reported an elastic electroactive hydrogel-based device able to maintain high electrical conductivity under substantial stretch and bending conditions. Specifically, chemical and anodic polymerizations were combined to obtain a tight bonding of a composite of PEDOT and polyurethane to an elastic double-network acrylamide hydrogel. The resulting hybrid disclosed excellent electrical conductivity ( $\sim 120 \text{ S cm}^{-1}$ ), which was maintained after six months.<sup>14</sup>

In recent studies we developed poly- $\gamma$ -glutamic acid ( $\gamma$ PGA) biohydrogels for energy storage applications.<sup>27,28</sup>  $\gamma$ PGA is an anionic homopolypeptide linked by the peptide bond between the  $\alpha$ -amino and the  $\gamma$ -carboxyl groups of glutamic acid,<sup>29</sup> which exhibits good biocompatibility, biodegradability, water-solubility and non-toxicity towards

humans.<sup>30</sup> This compound is produced from biosynthesis as a slime layer by a variety of members of the genus *Bacillus*.<sup>31</sup> Due to their robustness,  $\gamma$ PGA biohydrogels were used as solid electrolyte media for organic supercapacitors,<sup>27</sup> fulfilling the sustainability requirements of devices composed by naturally produced polymers.<sup>32</sup> More recently,  $\gamma$ PGA biohydrogels were combined with PEDOT microparticles using a new polymerization approach to fabricate flexible electrodes.<sup>28</sup> On the other hand, the combination of PEDOT with some inorganic fillers, as for example clays,<sup>33</sup> graphene,<sup>34,35</sup> carbon nanotubes,<sup>36</sup> and inorganic oxides,<sup>37,38</sup> results in an enhancement of capacitive and electrochemical properties. In a recent work, we proved that incorporation of alumina ( $\text{Al}_2\text{O}_3$ ) to PEDOT through in situ polymerization at pH 8.8 significantly improves the electrochemical activity of such EAP.<sup>39</sup>

In this work we combine our previous experience on  $\gamma$ PGA biohydrogels and  $\text{Al}_2\text{O}_3$  composites to develop a solid organic symmetric supercapacitor prototype containing the following elements: 1) two self-supported electrodes made of  $\gamma$ PGA, PEDOT microparticles, poly(hydroxymethyl-3,4-ethylenedioxythiophene) (PHMeDOT), which is a PEDOT derivative with an exocyclic hydroxyl group that facilitates its preparation in aqueous environments, and  $\text{Al}_2\text{O}_3$ ; and 2) a solid supporting electrolyte composed by  $\gamma$ PGA biohydrogel doped with  $\text{NaHCO}_3$ . The elements of the prototype have been synthesized, characterized and subsequently assembled using simple and low-cost techniques. The characterization of the supercapacitor prototype, which provides benefits as compactness, flexibility and lightweight, has been performed by cyclic voltammetry, electrochemical impedance spectroscopy and galvanostatic charging-discharging.

## **EXPERIMENTAL SECTION**

**Materials.** Free  $\gamma$ PGA from *Bacillus subtilis* ( $M_w = 350000$ ) was purchased from Wako Chemicals GmbH (Neuss, Germany). 1-[3-(Dimethylamino)propyl]-3-ethylcarbodiimide methiodide (EDC), cystamine dihydrochloride (Cys;  $\geq 98\%$ ), 3,4-ethylenedioxythiophene (EDOT), and hydroxymethyl-3,4-ethylenedioxythiophene (HMeDOT, 95%) were purchased from Sigma-Aldrich. EDOT and HMeDOT monomers were used as received.  $\text{NaHCO}_3$  and alumina were obtained from Panreac. Anhydrous  $\text{LiClO}_4$ , analytical reagent grade from Aldrich, was stored in an oven at  $70^\circ\text{C}$  before use in electrochemical experiments. Acetonitrile solvent was purchased from Sigma Aldrich. Milli-Q water grade ( $0.055\text{ S/cm}$ ) was used in all synthetic processes.

**Alumina microparticles.**  $\text{Al}_2\text{O}_3$  particles were prepared introducing the properly mass quantity into a vial containing magnetic stirrers, which was placed in a vortex at maximum power during 2 hours.<sup>39</sup> After that, particles were homogenized using a mortar. The size of the particles was controlled by both dynamic light scattering (DLS) and scanning electron microscopy (SEM).

**PEDOT microparticles.** PEDOT films were prepared by chronoamperometry at 1.40 V in an acetonitrile solution with 10 mM EDOT and 0.1 M  $\text{LiClO}_4$  as supporting electrolyte. The experimental set-up for this anodic polymerization was described in previous work.<sup>40</sup> PEDOT dispersed (20% w/w) in basic aqueous solution (0.5 M  $\text{NaHCO}_3$ ) was processed into particles using a vortex at maximum power during two hours. The size of the particles was controlled by both DLS and SEM. The resulting PEDOT particles were employed for the synthesis of loaded  $\gamma$ PGA hydrogels.

**Theoretical calculations.** The influence of the interaction between PEDOT and Al<sub>2</sub>O<sub>3</sub> particles in the electronic structure of the former has been examined by Density Functional Theory (DFT) calculations, which were performed using the Gaussian 09 computer package.<sup>41</sup> The geometries of the different investigated systems were fully optimized with the B3LYP<sup>42,43</sup> functional combined with the 6-31G(d) basis set. No symmetry constraints were used in the geometry optimizations.

The (001) and (010) surfaces of  $\gamma$ -Al<sub>2</sub>O<sub>3</sub> ( $P2_1/m$  space group, with  $a=5.587$  Å,  $b=8.413$  Å,  $c=8.068$  Å,  $\beta=90.59^\circ$ ) and the (001) surface of  $\alpha$ -Al<sub>2</sub>O<sub>3</sub> ( $R-3c$  space group with  $a=b=4.761$  Å,  $c=12.996$  Å) were represented without periodic boundary conditions but using relatively large slab models:  $3\times 2\times 1$  and  $3\times 1\times 2$  for the (001) and (010) surfaces of  $\gamma$ -Al<sub>2</sub>O<sub>3</sub>, and  $3\times 1\times 2$  for the (001) surface of  $\alpha$ -Al<sub>2</sub>O<sub>3</sub>. The interaction of these surfaces with a model molecule formed by two EDOT units (2-EDOT), which was considered in both neutral and oxidized state (dicationic form, 2-EDOT<sup>2+</sup>), was analyzed. Binding energies (BEs) were evaluated taking into account the standard counterpoise (CP) correction to eliminate the basis set superposition error (BSSE). The BE of the complex is defined as usual by subtracting the energy of the surface and the adsorbate from the energy of the complex.

**Preparation of PEDOT/Al<sub>2</sub>O<sub>3</sub>/γPGA solid electrode.** Flexible electrodes were prepared by *in situ* loading of PEDOT and Al<sub>2</sub>O<sub>3</sub> particles into γPGA biohydrogel (hereafter denoted PEDOT/Al<sub>2</sub>O<sub>3</sub>/γPGA).<sup>28</sup> In brief, γPGA and EDC were dissolved at 4 °C under magnetic stirring in 0.75 mL of 0.5 M NaHCO<sub>3</sub> containing 20% w/w and 2% w/w of PEDOT and Al<sub>2</sub>O<sub>3</sub> particles, respectively, relative to the weight of γPGA. After this, Cys was dissolved in 0.25 mL sodium hydrogen carbonate solution (0.5 M) and, subsequently, added to the solution and mixed during 2-3 minutes. The γPGA / EDC /

Cys molar ratio was 5 / 4 / 2. The final solution was stirred with a magnetic stirrer, and the reaction solution was poured into glass molds. The solution was let to gel at room temperature for one hour. To remove any compound in excess, the resulting loaded hydrogel was softly washed during 20 min with milli-Q water.

***Improvement of the PEDOT/Al<sub>2</sub>O<sub>3</sub>/γPGA electrodes by in situ polymerization of PHMeDOT.*** Steel AISI 316 sheets were coated with PEDOT/Al<sub>2</sub>O<sub>3</sub>/γPGA electrodes and subsequently kept for 24 h into a 10 mM HMeDOT aqueous solution with 0.1 M LiClO<sub>4</sub> at pH 8 under stirring (60 rpm). After this, PEDOT/Al<sub>2</sub>O<sub>3</sub>/γPGA coated sheets were used as working electrodes for the anodic polymerization of PHMeDOT by chronoamperometry using the same aqueous solution as reaction medium. Thus, in a previous study we demonstrated that PEDOT particles loaded into γPGA biohydrogel act as reaction nuclei for the electropolymerization of HMeDOT.<sup>28</sup> The anodic polymerization of HMeDOT monomers was conducted under a constant potential of 1.10 V using a polymerization time,  $\theta$ , of 2 hours, the resulting electrodes being denoted [PEDOT/Al<sub>2</sub>O<sub>3</sub>/γPGA]PHMeDOT.

The drastic reduction of  $\theta$  with respect to our previous work,<sup>28</sup> from 7 to 2 hours, is because the flexibility of the electrodes, which decreases with the content of PHMeDOT, has been prioritized with respect to the maximization of the electrochemical properties. Accordingly, the equilibrium between the loss in electrochemical properties and the gain in elastic behavior has been modulated with the electropolymerization time. In the specific case of [PEDOT/Al<sub>2</sub>O<sub>3</sub>/γPGA]PHMeDOT electrodes, we observed PEDOT microparticles join through grown PHMeDOT when  $\theta = 2$  h and, therefore, the supercapacitor reaches a high performance without detriment in the flexibility. [PEDOT/Al<sub>2</sub>O<sub>3</sub>/γPGA]PHMeDOT electrodes were used to construct

symmetric solid supercapacitors, as described below, using unloaded  $\gamma$ PGA biohydrogel as electrolytic medium.

***Preparation of  $\gamma$ PGA hydrogel as solid electrolyte and assembly of the symmetric cell.*** Pure  $\gamma$ PGA hydrogel for utilization as solid electrolyte was obtained using the same procedure described for [PEDOT/Al<sub>2</sub>O<sub>3</sub>/ $\gamma$ PGA]PHMeDOT electrodes. Thus, the only difference with respect to the preparation of such electrodes is that the 0.5 M NaHCO<sub>3</sub> solution used to dissolve the biopolymer was free of PEDOT and Al<sub>2</sub>O<sub>3</sub> particles. It is worth noting that the Na<sup>+</sup> ions coming from the NaHCO<sub>3</sub>, which neutralize the carboxylate groups that remain without crosslinking, act as a dopant when the prepared hydrogel is used as solid electrolyte in the supercapacitor prototype.

On the other hand, for the assembly of the supercapacitor prototype, the reaction solution used to prepare the  $\gamma$ PGA electrolyte was poured in a cylindrical container (1.2 cm length) that already contained a previously prepared [PEDOT/Al<sub>2</sub>O<sub>3</sub>/ $\gamma$ PGA]PHMeDOT electrode (cathode) of radius 0.45 cm. After five minutes, during the gelling process of the  $\gamma$ PGA electrolyte, the second [PEDOT/Al<sub>2</sub>O<sub>3</sub>/ $\gamma$ PGA]PHMeDOT electrode (anode) was added. This approach ensured the complete integration of the three elements of the cell through the electrolyte gelling reaction. Once the symmetric capacitor was assembled, it was soaked in milli-Q water during 2 h to remove any compound in excess coming from the gelation process.

***Chemical and physical characterization.*** Spectroscopic characterization of lyophilized hydrogels was conducted using FTIR spectroscopy. Morphological characterization of the electrodes was performed using SEM. The diameter of the particles was determined from the SEM images. The thermal stability was studied by

thermogravimetry analyses (TGA). Details about the equipment and operational conditions used for the characterization are provided in the Supplementary Information.

The swelling ratio (SR, %) of unloaded and loaded  $\gamma$ PGA hydrogels was determined according to:

$$SR = \frac{w_W - w_D}{w_D} \quad (3)$$

where  $w_W$  is the weight of the as prepared hydrogels after 30 min in milli-Q water and  $w_D$  is the weight of the hydrogels dried at room temperature during 30 min after preparation.

***Electrochemical characterization.*** All electrochemical experiments were run in triplicate using the  $\gamma$ PGA biohydrogel as solid supporting electrolyte. Cyclic voltammetry (CV) was carried out to evaluate the electroactivity, volumetric capacitance (VC) and specific capacitance (SC) of the capacitor and the electrochemical stability. Voltammograms were recorded considering different operational conditions: (a) Initial and final potential: 0.00 V; reversal potential: 0.80 V; scan rate: 50 mV/s; and (b) Initial and final potential: -0.50 V; reversal potential: 0.50 V; scan rate: 50, 100, 200 or 500 mV/s.

The SC (in mF/cm<sup>2</sup>) and the VC (in mF/cm<sup>3</sup>) were determined using the following expression:

$$SC = \frac{Q}{\Delta V \cdot A} \quad (4)$$

$$VC = \frac{Q}{\Delta V \cdot v} \quad (5)$$

where  $Q$  is voltammetric charge determined by integrating the oxidative (anodic charge) or the reductive parts (cathodic charge) of the cyclic voltammogram,  $\Delta V$  is the potential

window (in V),  $A$  is the area of the electrode (in  $\text{cm}^2$ ), and  $v$  is the total volume of the prototype.

The electrochemical stability was examined by evaluating the loss of electroactivity (LEA, in %) against the number of oxidation-reduction cycles:

$$LEA = \frac{\Delta Q}{Q_2} = \frac{Q_i - Q_2}{Q_2} \quad (6)$$

where  $\Delta Q$  is the difference between the oxidation charge (in C) of the second ( $Q_2$ ) and the evaluated oxidation-reduction cycle ( $Q_i$ ).

Galvanostatic charge-discharge (GCD) cycles were run using a current of 0.0035 mA. GCD curves were also employed to evaluate the  $SC$  and  $VC$  according to:

$$SC = \frac{\int I \cdot \Delta t}{\Delta V \cdot m} \quad (7)$$

$$SC = \frac{\int I \cdot \Delta t}{\Delta V \cdot v} \quad (8)$$

where  $I$  is the applied current,  $\Delta t$  is the time of discharge (in s),  $\Delta V$  is the difference between the potential at the beginning and at the end of the discharge (in V),  $m$  is the mass of the EAP (in g) and  $v$  is the volume of the symmetric capacitor (in  $\text{cm}^3$ ).

The energy and power density were calculated applying the following equations:

$$E = \frac{SCV^2}{2m} \quad (9)$$

$$P = \Delta V \frac{I}{m} \quad (10)$$

where  $SC$  is the specific capacitance (in mF/g considering the content of EAPs, *i.e.* PEDOT and PHMeDOT),  $V$  is the voltage at the beginning of the discharge (1.0 V),  $m$  is the mass of EAP,  $\Delta V$  is the difference between the potential at the beginning and at the end of the discharge,  $I$  is the applied current (0.0035 mA).

Electrochemical impedance spectroscopy (EIS) diagrams were taken at open circuit (OCP) over the frequency range of 100 kHz to 10 Hz with potential amplitude of 0.05 V using an AUTOLAB-302N potentiostat/galvanostat. All experiments were performed at room temperature using  $\gamma$ PGA as solid electrolyte. After data collection, EIS results were then processed and fitted to an electrical equivalent circuit (EEC). The percentage error associated with each circuit element was lower than 5%.

## RESULTS AND DISCUSSION

### Preparation and characterization of flexible electrodes and solid electrolyte

In order to improve the electrochemical performance of flexible PEDOT/ $\gamma$ PGA electrodes reported in previous work,<sup>28</sup>  $\text{Al}_2\text{O}_3$  microparticles were loaded into the biohydrogel using the procedure described in the Methods section. Homogenization and size reduction of  $\text{Al}_2\text{O}_3$  microparticles as obtained from synthesis (Figure 1a), which exhibited an averaged diameter of  $\sim 50 \mu\text{m}$ , was essential to ensure a good dispersion within the  $\gamma$ PGA matrix. After physical treatment,  $\text{Al}_2\text{O}_3$  particles with diameters ranging from  $\sim 1$  to  $\sim 10 \mu\text{m}$  were obtained (Figure 1b). PEDOT films (Figure 1c) were processed into particles of  $3.0 \pm 1.2 \mu\text{m}$  in diameter (Figure 1d-e). The successful incorporation of PEDOT and  $\text{Al}_2\text{O}_3$  particles inside the  $\gamma$ PGA hydrogel was corroborated by EDX, which enabled the detection of Al and S elements (Figure 1f).

In a recent study, we experimentally showed that the interaction of PEDOT and  $\text{Al}_2\text{O}_3$  particles favours considerably the electrochemical properties of the former.<sup>39</sup> In this work, theoretical DFT calculations on small complexes formed by 2-EDOT and different  $\text{Al}_2\text{O}_3$  clusters provide understanding of this phenomenon. Figure 2a displays the most stable complex obtained for the interaction of 2-EDOT with different  $\gamma$ - $\text{Al}_2\text{O}_3$  and  $\alpha$ - $\text{Al}_2\text{O}_3$  surfaces. The calculated BEs, which have been also included in Figure 2a,

indicate attractive and relatively strong interactions in all cases, even though the complex involving the (010) surface of  $\gamma$ - $\text{Al}_2\text{O}_3$  is the most favoured while that involving the (001) surface of  $\alpha$ - $\text{Al}_2\text{O}_3$  is the least attractive. As it was expected, interactions in complexes with 2-EDOT<sup>+2</sup> becomes more attractive, the BEs increasing by about 25-27% for  $\gamma$ - $\text{Al}_2\text{O}_3$  and 169% for  $\alpha$ - $\text{Al}_2\text{O}_3$ , as is reflected by the values included in Figure 2a.

Figure 2b represents the C–C bond length alternation patterns of 2-EDOT and 2-EDOT<sup>+2</sup> molecules alone, which are consistent with the expected benzenoid- and quinoid-like pattern, respectively.<sup>44</sup> However, the interaction with the (010) and (001) surfaces of  $\gamma$ - $\text{Al}_2\text{O}_3$  causes drastic changes in the electronic structure of the dimer. This is reflected in Figure 2b that includes the corresponding bond length alternation patterns. Thus, all C–C bond lengths adopt a value of  $\sim 1.40$  Å with exception of the two terminal bonds, evidencing the delocalization of the  $\pi$ -aromatic system. This phenomenon, which is practically identical for both 2-EDOT and 2-EDOT<sup>+2</sup> and has been attributed to the transfer of electrons from the organic molecule to the mineral, explains the enlargement of electric conductivity and capacitance when PEDOT and  $\gamma$ - $\text{Al}_2\text{O}_3$  are combined. In contrast, the typical benzenoid and quinoid-like patterns are preserved in the complexes with  $\alpha$ - $\text{Al}_2\text{O}_3$ , revealing the importance of the mineral's structure. In this work, PEDOT/ $\text{Al}_2\text{O}_3$ / $\gamma$ PGA and [PEDOT/ $\text{Al}_2\text{O}_3$ / $\gamma$ PGA]PHMeDOT electrodes have been prepared using  $\gamma$ - $\text{Al}_2\text{O}_3$ , as is proved below by FTIR spectroscopy.

The electrochemical behaviour of PEDOT/ $\text{Al}_2\text{O}_3$ / $\gamma$ PGA was enhanced by incorporating PHMeDOT inside the hydrogel through the anodic polymerization of HMeDOT monomers in aqueous solution. In order to ensure the penetration of the monomers into the hydrogel matrix and, therefore, their access to the PEDOT particles, which act as polymerization nuclei, PEDOT/ $\text{Al}_2\text{O}_3$ / $\gamma$ -PGA was kept under stirring in the

reaction medium during 24 h. It is worth noting that, although the electroactivity and *SC* of PHMeDOT and PEDOT are very similar, the solubility of HMeDOT in water is higher than that of EDOT. Accordingly, the incorporation of PHMeDOT inside the hydrogel, growing from loaded EAP microparticles, is expected to improve the electrochemical characteristics of PEDOT/Al<sub>2</sub>O<sub>3</sub>/γPGA without cause detriment in the properties already induced by PEDOT.<sup>28</sup> The *in situ* polymerization of HMeDOT resulted in the formation of continuous electroactive structures, which can be described as networks of micrometric PHMeDOT aggregates connected through relatively long ultra-thin sticks. This is illustrated in Figure 1g, which displays a representative SEM micrograph of the prepared [PEDOT/Al<sub>2</sub>O<sub>3</sub>/γPGA]PHMeDOT electrode. The organization of PHMeDOT in networks of clusters and sticks resembles the one achieved for PEDOT using short polymerization times,<sup>45</sup> which is also consistent with the morphological similarity between PEDOT and PHMeDOT micrometric films.<sup>46,47</sup>

Figure 3a compares the FTIR spectra of the [PEDOT/Al<sub>2</sub>O<sub>3</sub>/γPGA]PHMeDOT electrode and the γPGA electrolyte. Both spectra show the typical bands of the γPGA biohydrogel, which were already compared with those of the biopolymer before the cross-linking reaction.<sup>27</sup> In brief, the most characteristic trend corresponds to the formation of –CONH– bonds due to the reaction between the γPGA chains and the cross-linker, which was identified by the enhancement of both the amide I (1621 cm<sup>-1</sup>) and amide II (1530 cm<sup>-1</sup>) bands and the disappearance of the free carboxylic acid (1718 cm<sup>-1</sup>) and asymmetric COO<sup>-</sup> bands (1595 cm<sup>-1</sup>). On the other hand, the presence of PEDOT and PHMeDOT in the electrode is evidenced by the C–O–C (1090 cm<sup>-1</sup>) and ethylenedioxy (1180 cm<sup>-1</sup>) stretching vibrations as well the shift of the broad band identified at 3298 cm<sup>-1</sup> for the γPGA electrolyte (overlapping of N–H and O–H stretching bands) towards 3258 cm<sup>-1</sup> in the electrode due to the increment in the amount

of hydroxyl groups arising from PHMeDOT. In addition, the bands at  $1092\text{ cm}^{-1}$  (Al–O–H bending) and at  $900$  and  $1100\text{ cm}^{-1}$  (Al–O–H deformations) reflect the incorporation of alumina, which converts into  $\text{Al}(\text{OH})_3$  because of the basic pH. The latter is corroborated by the band at  $3092\text{ cm}^{-1}$ , which is used as a fingerprint of the –OH groups in  $\gamma$ -alumina.<sup>48</sup>

The thermal stabilities of  $\gamma$ PGA, PEDOT/ $\text{Al}_2\text{O}_3$ / $\gamma$ PGA and [PEDOT/ $\text{Al}_2\text{O}_3$ / $\gamma$ PGA]PHMeDOT are compared in Figure 3b, which displays the TGA and DGTA curves. The different shape of the TGA curves indicates that the degradation mechanism of the biohydrogel is affected by the loading. The initial loss of weight at  $\sim 100\text{ }^\circ\text{C}$ , which is ascribed to the evaporation of water absorbed in the  $\gamma$ PGA network, occurs in a different way for the electrodes than for the supporting electrolyte. Comparison of the PEDOT/ $\text{Al}_2\text{O}_3$ / $\gamma$ PGA and [PEDOT/ $\text{Al}_2\text{O}_3$ / $\gamma$ PGA]PHMeDOT curves with those previously reported for PEDOT/ $\gamma$ PGA and [PEDOT/ $\gamma$ PGA]PHMeDOT indicates that alumina acts as a thermos-resistant glue, making difficult the evaporation of water. The decomposition process starts at temperatures higher than  $200\text{ }^\circ\text{C}$  for all samples, even though differences in the weight loss reveals that alumina has a delaying effect in the decomposition of the electrodes. However, the degradation process becomes more complex upon the incorporation of PEDOT, alumina and PHMeDOT, as is evidenced by the multiple peaks surrounding the one associated to the maximal decomposition in the DTG curves. Overall, these results prove that alumina particles enhance the thermal resistance of the proposed electrodes.

Swelling tests indirectly prove the importance of the presence of  $\text{NaHCO}_3$  during the preparation of the  $\gamma$ PGA that, in addition to providing  $\text{Na}^+$  ions capable of moving inside the biohydrogel, helps to maintain the dimensional stability of the electrode. Figure S1 compares the temporal evolution of the swelling ratio (Eqn 3) for

[PEDOT/Al<sub>2</sub>O<sub>3</sub>/γPGA]PHMeDOT electrode when immersed in pure milli-Q water and in 0.5 M NaHCO<sub>3</sub> aqueous solution. After 3 hours, the swelling is 83% and 15%, respectively, demonstrating that the incorporation of NaHCO<sub>3</sub> during the synthetic process contributes to the dimensional stability. Thus, the Na<sup>+</sup> cations of the salt neutralize the negatively charged carboxylate groups from γPGA, reducing their hydration capacity of the hydrogel and contributing to the volumetric stability of both the electrodes and the solid electrolyte.

### **Assembly and optimization of the symmetric supercapacitor prototype**

The compact supercapacitor was built by connecting two [PEDOT/Al<sub>2</sub>O<sub>3</sub>/γPGA]PHMeDOT electrodes, which acted as cathode (C) and anode (A), through a solid electrolyte (SE) made of γPGA biohydrogel, as is schematically represented in Figure 4a. In order to obtain a very robust prototype, already prepared electrodes were assembled to the electrolyte during its gelling reaction, as is described in the Methods section. A photograph of the prototype is displayed in Figure 4b. The very high flexibility of the individual assembled elements, which is illustrated in Figures 4c and 4d for the electrode and the electrolyte, respectively, resulted in a supercapacitor with outstanding mechanical properties. In addition to the flexibility, the very high compressibility of the supercapacitor deserves special mention. This is illustrated in Figure 4e that proves compressibility higher than 100%. Other interesting characteristics of the supercapacitor prototypes are: small and controllable dimensions (see below), manageability, portability, robustness and lightweight. Figure 4f displays the connections used to conduct electrochemical experiments and evaluate the performance of the prototype.

The dimension of the supercapacitor prototype could be a relevant factor in terms of final application and specific properties requested (flexibility and elasticity). In order to find the best compromise between size and electrochemical performance, CV assays were conducted on prototypes with different electrode and solid electrolyte lengths. The effect of the amount of EAP on the  $SC$  (Eqn 4) was investigated by changing the length of the electrode, whereas the separation between the electrodes (*i.e.* solid electrolyte length) was used to examine the influence of the path travelled by the ions across the gel on the  $VC$  (Eqn 5).

It should be remarked that because of the symmetric supercapacitor configuration, the length of the two electrodes, the cathode and the anode, ( $w_c$ ) is identical. Figure 5a represents the variation of the  $SC$  against the scan rate for supercapacitor prototypes in which  $w_c$  is 2 or 4 mm, while the length of the solid electrolyte ( $w_s$ ) is kept at 2 mm. As it can be seen, the increment of the  $SC$  with content of EAP is higher than expected, since when  $w_c$  changes from 2 to 4 mm, the  $SC$  increases more than double (*i.e.* from 3.8 to 10.8 mF/g). On the other hand, the change of  $VC$  with the scan rate was examined considering four different cases, in which variations in  $w_c$  and  $w_s$  occur simultaneously: (i)  $w_c = w_s = 2$  mm; (ii)  $w_c = 2$  mm and  $w_s = 4$  mm; (iii)  $w_c = w_s = 4$  mm; and (iv)  $w_c = 4$  mm and  $w_s = 8$  mm. Figure 5b indicates that  $VC$  decreases with increasing  $w_s$ , independently of  $w_c$  (*i.e.* from 0.06 to 0.03 mF/cm<sup>3</sup> when  $w_s$  increases from 2 to 4 mm for  $w_c = 2$  mm, and from 0.11 to 0.09 mF/cm<sup>3</sup> when  $w_s$  increases from 4 to 8 mm for  $w_c = 4$  mm). On the basis of these results, the optimum values chosen for the supercapacitor prototype, and used for the devices characterized in next sections, were  $w_c = w_s = 4$  mm (*i.e.* total length 1.2 cm, Figure 3a).

### **Optimization of the electrical double layer capacitive behavior**

Once the lengths of the electrodes and the solid electrolyte have been optimized, the capacitive behavior of the prototype is improved by adjusting the potential window used in CV assays. Cyclic voltammograms recorded in the potential interval comprised between 0.00 (initial/final potential) and 0.80 V (reversal potential) do not approximate to the desired rectangular or quasi-rectangular shape (Figure S2), which has been attributed to the irreversible oxidation peak typically found in polythiophene derivatives at around 0.8 V.<sup>49,50</sup> In order to enhance the double layer capacitive behaviour of the device, different operation potential windows were considered. More specifically, CV assays were performed, on one side, by reducing the reversal potential from 0.80 V to 0.70, 0.60 and 0.50 V while the initial/final potential was kept at 0.00 V and, on the other side, by decreasing the initial/final potential from 0.00 V to -0.10 and -0.30 V while the reversal potential was kept at 0.80 V.

The influence of the irreversible oxidation peak in the distortion of the CV curves from the near-rectangular shape decreased by reducing the reversal potential (Figure S3), even though the *SC* decreased from 10.8 mF/g to 3.3 mF/g. Similarly, when the initial/final potential is moved towards lower values the curve approximates more to the desired rectangular shape (Figure S4). On the basis of these electrochemical assays, the operation potential window was defined by -0.50 V as initial/final potential and 0.50 V as reversal potential. Cyclic voltammograms from -0.50 to 0.50 V, which are displayed in Figure 6a, shows an almost ideal rectangular shape for scan rates up to 500 mV/s, evidencing good capacitive performance, high rate capability, low contact resistance and the absence of Faradaic reactions. The *SC* determined using such potential window and a scan rate of 50 mV/s was 3.3 mF/g. This value decreases with increasing scan rate (*e.g.* *SC*= 2.2 mF/g when the scan rate increases to 500 mV/s), which has been attributed to a progressively less efficient infiltration of the ions into the porous matrix.

Thus, at slow scan rates, the diffusion of ions from the electrolyte can gain access to almost all available pores of the electrodes, favoring their penetration and leading to a higher  $SC$  values. Indeed, application of Cottrell model (Figure S5) corroborates that ion motions through the complex structures of the porous 3D electrodes and solid electrolyte depend only on the diffusion. Overall, the  $SC$  values obtained for the supercapacitor prototype, which ranged from 10.8 to 2.2 mF/g depending on the potential window and the scan rate, are comparable not only to those of ordinary commercial capacitors (in the order of mF/g) but also to those based on porous carbonaceous structures, as for example carbon-based graphitic nanoweb (from 8.9 to 1.1 mF/g),<sup>51</sup> activated carbon cloth (8.8-0.8 mF/g),<sup>52</sup> and graphene oxide nanocapsules with silanized hydrogels (100 mF/g).<sup>53</sup>

### **Electrochemical performance of the prototype**

In addition to previously discussed CV results, the performance of the supercapacitor device was analyzed using GCD cycles and EIS. Figure 6b shows the first GCD curves (charging and discharging times of 20 and 10 s, respectively) recorded at 0.0035 mA, which corresponds to the average of the oxidation and reduction currents observed in cyclic voltammograms at scan rate of 100 mV/s (Figure 6a). As it can be seen, charge-discharge curves are almost linear and symmetric, while the cell potential increases slowly (*e.g.* from 0.87 to 0.93 V after 10 cycles). After ~300 cycles the cell potential reaches a value of 1.02 V (inset in Figure 6b) that is preserved until the last cycle. Thus, the system reaches a steady state, as is detailed in the magnified plot associated to the last few cycles from a total of 2000 GCD cycles (Figure 6b, right). Along this process, the  $SC$  decreases from 4.8 mF/g (2nd cycle) to 4.4 mF/g, which represents 92% of

retention. These results point out not only the good electrochemical performance of the device but also its high cyclability.

The 8% loss of  $SC$  after 2000 GCD cycles suggests that some structural changes in the electrodes and/or solid electrolyte. Thus, swelling and shrinkage processes may alter the structure of the pores, affecting the access and/or scape of ions. Figure 7 compares SEM micrographs of the different elements of the prototype before and after applying 2000 GCD cycles, evidencing the structural aging of the different elements assembled in the prototype. Specifically, charge-discharge processes affect the porous structure of the two electrodes, even though in a different way. Specifically, in the cathode pores become more irregular, open and heterogeneous after 2000 GCD cycles, while in the anode pores tend to collapse and, therefore, display a significant size reduction. Besides, inspection of the  $\gamma$ PGA solid electrolyte reveals the dehydration of the biohydrogel during the charge-discharge cycles. Accordingly, the wide and well-defined pores observed in the fresh electrolyte have been converted into relatively closed channels, making more difficult the motion of the ions.

On the other hand, the  $SC$  decreases with increasing current density (Figure 8a). The accumulation of ions at the outer surface of the electrodes increases with the current density, explaining the reduction of the  $SC$ . As it can be seen, when the current density increases from 0.5 to 1 mA/g, the rate of decrease of the  $SC$  is lower than that from 0.2 to 0.3 mA/g. Therefore, the prototype can be used at the highest current density while the  $SC$  is still as high as 2.2 mF/g. However, in order to take more advantage of the porous structure of the supercapacitor, low current densities are recommendable. These observations are supported by Figure 8b, which represents the variation of the energy density ( $E$ ; Eqn 9) against the power density ( $P$ ; Eqn 10) for different discharging

current densities (0.2, 0.3, 0.5 and 1.0 mA/g). As it can be seen,  $E$  decreases gradually with increasing  $P$ , proving the superficial accumulation of charge.

EIS studies were conducted to determine the electrical conductivity of the supercapacitor. Accordingly, the impedance was measured for frequencies ranging from 10 to  $10^5$  Hz using a recently developed through-plane impedance cell (Figure 8c).<sup>54</sup> The Nyquist plot and the electric equivalent circuit (EEC) are displayed in Figures 8d and 8e, respectively. The almost straight line observed in the profile suggests a Warburg-like behavior, which is characteristic of electrical double-layer porous capacitors.<sup>55</sup> At high frequencies, the plot shows a very soft semicircle, indicating a fast charge transfer through a Faradaic process with negligible charge transfer resistance. This is consistent with the porous structure of the electrode, which favors the permeation of the electrolyte and enhances the ion transfer kinetics.<sup>56</sup>

The Randles-Ershler EEC model used for fitting the experimental data from EIS measurements provides not only understanding of the response of the fundamental systems with coupled processes (*e.g.* charge transfer, diffusion, electric double layer charging and uncompensated solution resistance) but also quantification of some fundamental interfacial phenomena. The solid electrolyte resistance ( $R_e$  in Figure 8e), which arises from the  $\text{NaHCO}_3$  salt used during synthesis of the biohydrogel, is 35  $\Omega$ . This corresponds to an ionic conductivity of  $4.5 \cdot 10^{-3}$  S/cm, reflecting the semiconducting behavior of the prototype. This is consistent with the  $E$  vs  $P$  graphic (Figure 8b) discussed above. On the other hand, the value of the charge-transfer resistance ( $R_{ct} = 40 \Omega$ ) is very similar to  $R_e$ , facilitating the exchange of ions along the double layer. The  $R_{ct}$  is in series with a constant phase element (CPE) impedance, as is typically observed in gel-based electrodes.<sup>57</sup> The CPE impedance has been expressed as:

$$Z_{\text{CPE}} = \frac{1}{Y_0(j\omega)^n} \quad (9)$$

where  $Y_0$  is the admittance of an ideal capacitance and  $n$  is an empirical constant ranging from 0 to 1. The CPE represents a capacitor and a resistor for  $n= 1$  and  $n= 0$ , respectively, while it is associated with a diffusion process when  $n= 0.5$  and is equivalent to the so-called Warburg element. In this work, the  $Z_{\text{CPE}}$  with  $n= 0.77$  is related with the ionic diffusion through the electrode. Finally, the double layer capacitance element ( $C_{\text{dl}}$ ), with a value of  $4.12\mu\text{F}$ , reflects the capacitance at the electrode/electrolyte interphase. The quality of the experimental data fitting to EEC was evaluated to estimate the percentage error associated with each circuit element, being comprised between 1.5% and 4.1% in all cases.

## CONCLUSIONS

Flexible, compact, lightweight and biocompatible symmetric supercapacitors have been developed by assembling two identical electrodes, constituted by EAPs- and alumina-containing electroactive hydrogels, through a  $\gamma$ PGA biohydrogel doped with  $\text{NaHCO}_3$ , which act as a solid electrolyte. After optimization, the best configuration of the prototype exhibits the following characteristics: 4 mm as length of the electrodes, 4 mm as length of the solid electrolyte, working potential window that expands from -0.50 V to 0.50 V at a scan rate of 100 mV/s. The galvanostatic  $SC$  of the prepared supercapacitors is 4.8 mF/g, a good  $E$  ( $4.6 \cdot 10^{-4}$  mWh/g $^{-1}$ ) and cyclability (92% of retention of the specific capacitance after 2000 GCD cycles) being achieved. The excellent electrochemical properties of PEDOT and PHMeDOT, which are enhanced in presence of alumina, in combination with the mechanical strength and flexibility of the

$\gamma$ PGA biohydrogel, suggest the supercapacitor prototype prepared in this work is a promising energy storage device.

## ACKNOWLEDGEMENTS

Authors acknowledge MINECO/FEDER (MAT2015-69367-R and MAT2015-69547-R) and the Agència de Gestió d'Ajuts Universitaris i de Recerca (2017SGR359) for financial support. M.S.G is grateful to Costa Rica National Commission of Scientific and Technological Research (CONICYT-Support N°FI-172B-14). Support for the research of C.A. was received through the prize “ICREA Academia” for excellence in research funded by the Generalitat de Catalunya.

## REFERENCES

1. C. Y. Wang, A. M. Ballantyne, S. B. Hall, C. O. Too, D. L. Officer and G. G. Wallace, *J. Power. Sources.*, 2006, **156**, 610–614.
2. X. Wang, X. Lu, B. Liu, D. Chen, Y. Tong and G. Shen, *Adv. Mater.*, 2014, **26**, 4763–82.
3. Y. Zhao, B. Liu, L. Pan and G. Yu, *Energy. Environ. Sci.*, 2013, **6**, 2856–2870.
4. Y. Shi and G. Yu, *Chem. Mater.*, 2016, **28**, 2466–2477.
5. Y. Shi, L. Peng, Y. Ding, Y. Zhao and G. Yu, *Chem. Soc. Rev.*, 2015, **44**, 6684–6696.
6. J. Kim, J. Lee, J. You, M. Park, S. Al. Hossain and J. Ho, *Mater Horizons.*, 2016, **3**, 517–535.
7. B. C. Kim, G. M. Spinks, G. G. Wallace and R. John, *Polymer*, 2000, **41**, 1783–1790.

8. S. Brahim, D. Narinesingh and A. Guiseppi-Elie, *Biosens. Bioelectron.*, 2002, **17**, 53–59.
9. S. Brahim, D. Narinesingh and A. Guiseppi-Elie, *Biosens. Bioelectron.*, 2002, **17**, 973–981.
10. A. Guiseppi-Elie, *Biomaterials*, 2010, **31**, 2701–2716.
11. U. Lange, N. V. Roznyatovskaya and V. M. Mirsky, *Anal. Chim. Acta*, 2008, **614**, 1–26.
12. R. Balint, N. J. Cassidy and S. H. Cartmell, *Acta. Biomater.*, 2014, **10**, 2341–2353.
13. J. G. Hardy, J. Y. Lee and C. E. Schmidt, *Curr. Opin. Biotechnol.*, 2013, **24**, 847–854.
14. M. Sasaki, B. C. Karikkineth, K. Nagamine, H. Kaji, K. Torimitsu and M. Nishizawa, *Adv. Health. Mater.*, 2014, **3**, 1919–1927.
15. L. M. Lira, R. Barthus and S. Torresi, *ECS Transactions.*, 2007, **3**, 105–114.
16. H. Lee, W. Hong, S. Jeon, Y. Choi and Y. Cho, *Langmuir*, 2015, **31**, 4264–4269.
17. M. Asplund, T. Nyberg and O. Inganäs, *Polym. Chem.*, 2010, **1**, 1374–1391.
18. G. Justin and A. Guiseppi-Elie, *Biomacromolecules*, 2009, **10**, 2539–2549.
19. D. Mawad, A. Lauto and G. G. Wallace, Conductive Polymer Hydrogels. In *Polymeric Hydrogels as Smart Biomaterials*. S. Kalia, (Ed.); Springer, 2016; pp 19–45.
20. G. A. Snook, P. Kao and A. S. Best, *J. Power Sources*, 2011, **196**, 1–12.
21. Y. Shi, L. Peng and G. Yu, *Nanoscale*, 2015, **7**, 12796–12806.
22. L. Pan, G. Yu, D. Zhai, H. Ryoung, W. Zhao, N. Liu, H. Wang, B. C.-K. Tee, Y. Shi, Y. Cui and Z. Bao, *Proc. Natl. Acad. Sci. (USA)*, 2012, **109**, 1–6.
23. C. A. Mire, G. G. Wallace and P. Calvert, *J. Mater. Chem.*, 2011, **21**, 2671–2678.

24. A. C. Glavan, S. B. Walker, J. A. Lewis, G. M. Whitesides and C. Link, *Adv. Mat.*, 2017, **26**, 4677–4682.
25. T. Boland, T. Xu, B. Damon and X. Cui, *Biotechnol. J.*, 2006, **1**, 910–917.
26. S. Sekine, Y. Ido, T. Miyake, K. Nagamine and M. Nishizawa, *J. Am. Chem. Soc.*, 2010, **132**, 13174–13175.
27. M. M. Pérez-Madrigal, M. G. Edo, A. Díaz, J. Puiggali and C. Alemán, *J. Phys. Chem. C.*, 2017, **121**, 3182–3193.
28. M. C. G. Saborío, S. Lanzalaco, G. Fabregat, J. Puiggali, F. Estrany and C. Aleman, *J. Phys. Chem. C*, 2018, **122**, 1078–1090.
29. I. Bajaj and R. Singhal, *Bioresour. Technol.*, 2011, **102**, 5551–5561.
30. I. Shih, P. Wu and C. Shieh, *Process Biochem.*, 2005, **40**, 2827–2832.
31. C. B. Thome, C. G. Gómez, H. E. Noyes and R. D. Housewright, *J. Bacteriol.*, 1954, **68**, 307–315.
32. E. Armelin, M. M. Perez-Madrigal, C. Alemán and D. D. Díaz-Díaz, *J. Mater. Chem. A*, 2016, **4**, 8952–8968.
33. X. Bai, X. Hu and S. Zhou, *RSC Adv.*, 2015, **5**, 43941–43948.
34. C. Chen, T. Zhang, Q. Zhang, X. Chen, C. Zhu, Y. Xu, J. Yang, J. Liu and D. Sun, *ACS Appl. Mater. Interfaces*, 2016, **8**, 10183–10192.
35. W. Lee, Y. H. Kang, J. Y. Lee, K-S. Jang and S. Y. Cho, *RSC Adv.*, 2016, **6**, 53339–53344.
36. R. Ramakrishnan, S. J. Devaki, S. Thomas, M. R. Varma and K. P. P. Naajiya, *J. Phys. Chem. C.*, 2016, **120**, 4199–4210.
37. C. X. Guo, G. Yilmaz, S. Chen, S. Chen and X. Lu, *Nano Energy*, 2015, **12**, 76–87.
38. Z. H. Wang, P. Tammela, J. Huo, P. Zhang, M. Strømme and L. Nyholm, *J. Mater. Chem. A*, 2016, **4**, 1714–1722.

39. M. C. G. Saborío, F. Estrany and C. Alemán, *J. Polym. Sci. Part B: Polym. Phys.*, 2017, **55**, 1131–1141.
40. C. Ocampo, R. Oliver, E. Armelin, C. Alemán and F. Estrany, *J. Polym. Res.*, 2006, **13**, 193–200.
41. M. J. Frisch, G. W. Trucks, H. B. Schlegel, G. E. Scuseria, M. A. Robb, J. R. Cheeseman, G. Scalmani, V. Barone, B. Mennucci, G. A. Petersson, H. Nakatsuji, M. Caricato, X. Li, H. P. Hratchian, A. F. Izmaylov, J. Bloino, G. Zheng, J. L. Sonnenberg, M. Hada, M. Ehara, K. Toyota, R. Fukuda, J. Hasegawa, M. Ishida, T. Nakajima, Y. Honda, O. Kitao, H. Nakai, T. Vreven, J. A. Jr Montgomery, J. E. Peralta, F. Ogliaro, M. Bearpark, J. J. Heyd, E. Brothers, K. N. Kudin, V. N. Staroverov, R. Kobayashi, J. Normand, K. Raghavachari, A. Rendell, J. C. Burant, S. S. Iyengar, J. Tomasi, M. Cossi, N. Rega, J. M. Millam, M. Klene, J. E. Knox, J. B. Cross, V. Bakken, C. Adamo, J. Jaramillo, R. Gomperts, R. E. Stratmann, O. Yazyev, A. J. Austin, R. Cammi, C. Pomelli, J. W. Ochterski, R. L. Martin, K. Morokuma, V. G. Zakrzewski, G. A. Voth, P. Salvador, J. J. Dannenberg, S. Dapprich, A. D. Daniels, O. Farkas, J. B. Foresman, J. V. Ortiz, J. Cioslowski and D. J. Fox, *Gaussian 09, revision A.01*, Gaussian, Inc.: Wallingford, CT, 2009.
42. C. Lee, W. Yang and R. G. Parr, *Phys. Rev. B*, 1988, **37**, 785–789.
43. A. D. Becke, *J. Chem. Phys.* 1993, **98**, 5648–5652.
44. J. Casanovas and C. Alemán, *J. Chem. Phys.* 1993, **98**, 5648–5652.
45. D. Aradilla, F. Estrany, E. Armelin and C. Alemán, *Thin Solid Films*, 2012, **520**, 4402–4409.
46. G. Fabregat, J. Casanovas, E. Redondo, E. Armelin and C. Alemán, *Phys. Chem. Chem. Phys. C*, 2007, **111**, 4823–4830.

47. M. A. Hocevar, G. Fabregat, E. Armelin, C. A. Ferreira and C. Alemán, *Eur. Polym. J.*, 2016, **79**, 132–139.
48. L. A. Prado, M. Sriyai, M. Ghislandi, A. Barros-Timmons and K. Schulte, *J. Braz. Chem. Soc.*, 2010, **21**, 2238–2245.
49. B. Teixeira-Dias, L. J. del Valle, D. Aradilla, F. Estrany and C. Alemán, *Macromol. Mater. Eng.*, 2012, **297**, 427–436.
50. G. G. Láng, M. Ujvári, S. Vesztergom, V. Kondratiev, J. Gubicza and K. J. Szekeres, *Int. J. Research in PCCP*, 2016, **230**, 1281–1302.
51. Y. S. Yun, *Nanoscale Res. Lett.*, 2018, **13**, 36.
52. G. Wang, H. Wang, X. Lu, Y. Ling, M. Yu, T. Zhai, Y. Tong and Y. Li, *Adv. Mater.*, 2014, **26**, 2676–2682.
53. R. Katakya, J. H. L. Hadden, K. S. Coleman, C. N. M. Ntola, M. Chowdhury, A. R. Duckworth, B. P. Dobson, R. Campos, S. Pyner and F. Shenton, *Chem. Commun.*, 2015, **51**, 10345–10348.
54. F. Müller, C. A. Ferreira, D. S. Azambuja, C. Alemán and E. Armelin, *J. Phys. Chem. B*, 2014, **118**, 1102–1112.
55. Z. Niu, W. Zhou, J. Chen, G. Feng, H. Li, W. Ma, J. Li, H. Dong, Y. Ren, D. Zhao and S. Xie, *Energy Environ. Sci.*, 2011, **4**, 1440–1446.
56. M. Ujvári, M. Takács, S. Vesztergom, F. Bazsó, F. Ujhelyi and G. G. Láng, *J. Solid State Electrochem.*, 2011, **15**, 2341–2349.
57. H. Warrena and M. Panhuis, *Proc. of SPIE.*, 2014, **9171**, 3–8.

## CAPTIONS TO FIGURES

**Figure 1.** (a-d) SEM micrographs of: alumina particles (a) before and (b) after the physical treatment; and (c) PEDOT film and (d) PEDOT microparticles. (e) Histogram derived from SEM measurements showing the diameter of PEDOT microparticles. (f) EDX spectrum and (g) SEM micrograph of the [PEDOT/Al<sub>2</sub>O<sub>3</sub>/γPGA]PHMeDOT electrode.

**Figure 2.** (a) Lowest energy complexes showing the interaction of 2-EDOT with the (001) and (010) surfaces of γ-Al<sub>2</sub>O<sub>3</sub> (top left and right, respectively) and the (001) surface α-Al<sub>2</sub>O<sub>3</sub> (bottom). Complexes with 2-EDOT<sup>+2</sup> are very similar and, therefore, are not depicted. The binding energy (BE) of each complex, including those with 2-EDOT<sup>+2</sup>, are indicated. (b) C–C bond distances along the conjugated π-systems of 2-EDOT (left) and 2-EDOT<sup>+2</sup> (right) alone (non-interacting) and interacting with Al<sub>2</sub>O<sub>3</sub> surfaces.

**Figure 3.** (a) FTIR spectra of γPGA and [PEDOT/Al<sub>2</sub>O<sub>3</sub>/γPGA]PHMeDOT. (b) TGA and DTGA curves of γPGA, PEDOT/Al<sub>2</sub>O<sub>3</sub>/γPGA and [PEDOT/Al<sub>2</sub>O<sub>3</sub>/γPGA]PHMeDOT.

**Figure 4.** (a) Scheme and (b) photograph of the assembled supercapacitor prototype. The length of the optimized prototype is displayed in (a). Photographs illustrating the flexibility of (c) the γPGA electrolyte and (d) [PEDOT/Al<sub>2</sub>O<sub>3</sub>/γPGA]PHMeDOT electrode. (e) Sequence of photographs displaying that the prototypes reaches a compression higher than 100%. (f) Connections used to conduct the electrochemical characterization of the supercapacitor prototype.

**Figure 5.** Optimization of the symmetric supercapacitor prototype: (a) Variation of the areal *SC* with the scan rate for devices prepared using electrodes of different length ( $w_c = 2$  or 4 mm) while the length of the solid electrolyte was kept at  $w_s = 2$  mm; (b)

Variation of the  $VC$  with the scan rate for devices prepared using different  $w_c$  and  $w_s$ . Both the  $SC$  and the  $VC$  were determined by CV: initial and final potential= 0.00 V; reversal potential: 0.80 V.

**Figure 6.** (a) Cyclic voltammograms of the supercapacitor prototype recorded at different scan rates comprised between 50 and 500 mV/s. Initial and final potentials: -0.50 V; reversal potential: 0.5 V. (b) GCD cycles recorded at 0.0035 mA (charging and discharging times: 20 and 10 s, respectively). The prototype was subjected to 2000 cycles (inset). Magnification of the first and last cycles is displayed.

**Figure 7.** SEM images of fresh [PEDOT/Al<sub>2</sub>O<sub>3</sub>/γPGA]PHMeDOT electrodes and γPGA solid electrolyte (left) and after structural aging by applying 2000 GCD cycles to the supercapacitor prototype.

**Figure 8.** (a) Variation of the  $SC$  (Eqn 7) as a function of current density. (b) Variation of  $E$  (Eqn 9) against  $P$  (Eqn 10) for the indicated discharging current densities. (c) Photograph of the supercapacitor prototype in the through-plane impedance cell used for EIS measurements. (d) Nyquist impedance plot showing the evolution of the impedance data of the supercapacitor prototype. (e) Equivalent circuit model used to fit the experimental data.

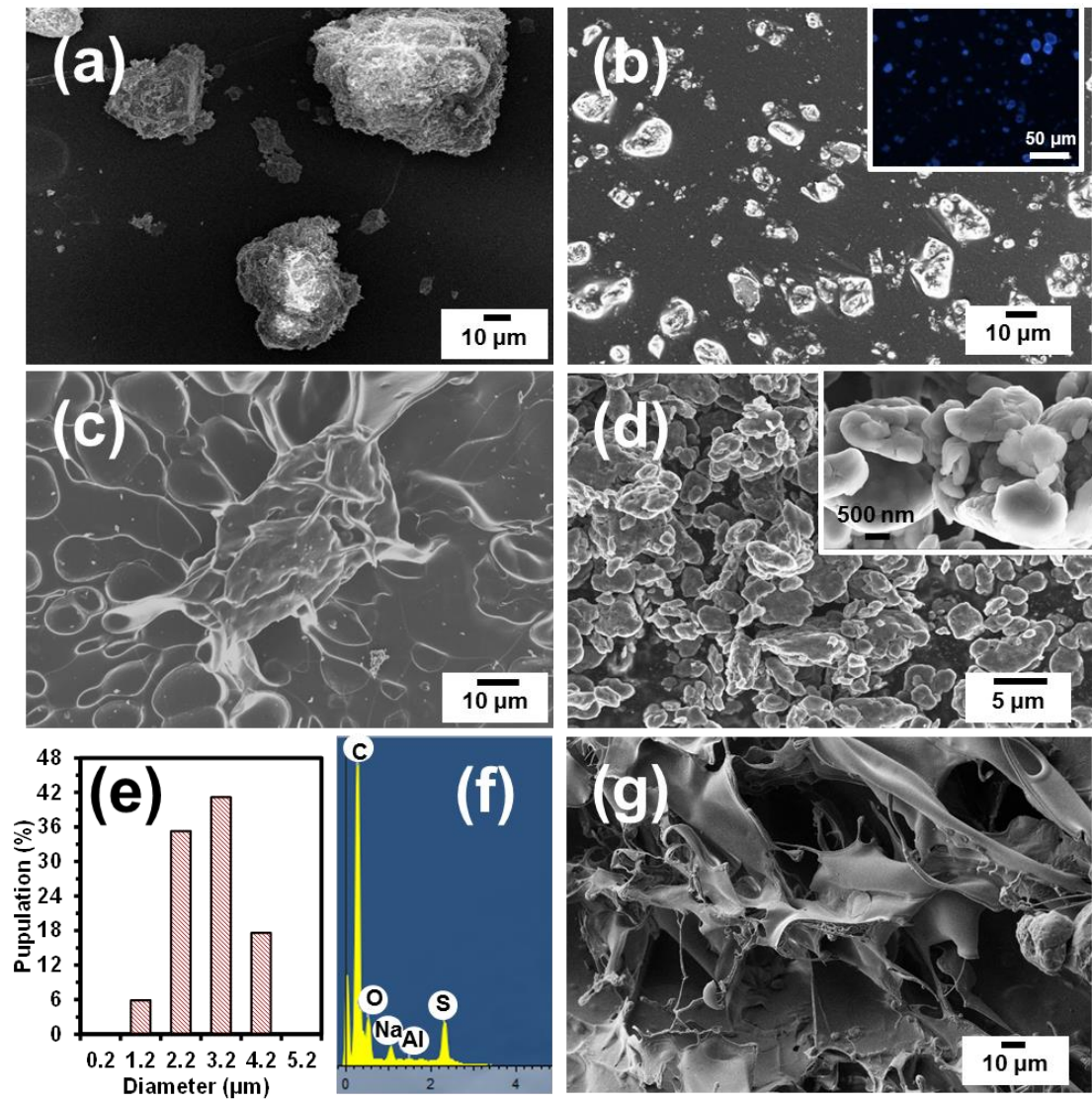
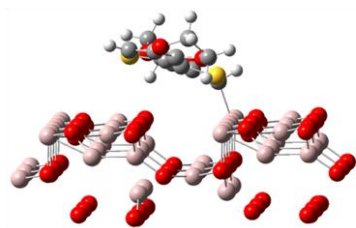


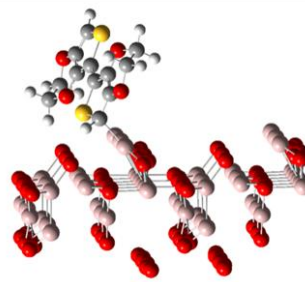
Figure 1

(a)



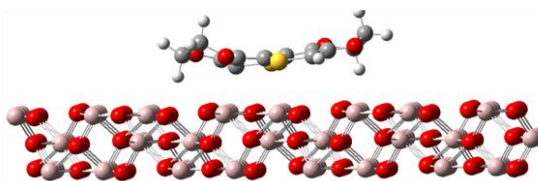
(001)  $\gamma$ - $\text{Al}_2\text{O}_3$ ...2-EDOT: -92.3 kcal/mol

(001)  $\gamma$ - $\text{Al}_2\text{O}_3$ ...2-EDOT<sup>+2</sup>: -115.7 kcal/mol



(010)  $\gamma$ - $\text{Al}_2\text{O}_3$ ...2-EDOT: -106.4 kcal/mol

(010)  $\gamma$ - $\text{Al}_2\text{O}_3$ ...2-EDOT<sup>+2</sup>: -135.7 kcal/mol



(001)  $\alpha$ - $\text{Al}_2\text{O}_3$ ...2-EDOT: -38.7 kcal/mol

(001)  $\alpha$ - $\text{Al}_2\text{O}_3$ ...2-EDOT<sup>+2</sup>: -104.2 kcal/mol

(b)

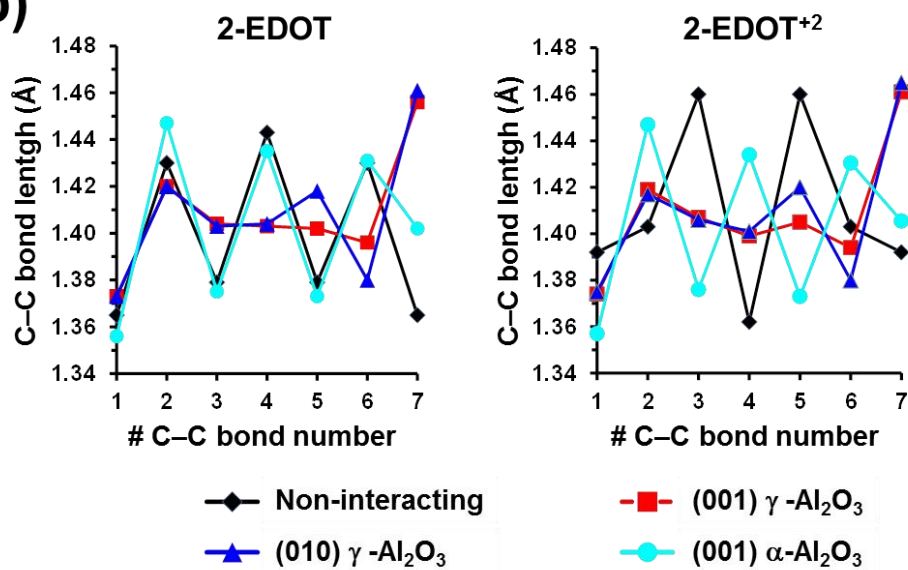


Figure 2

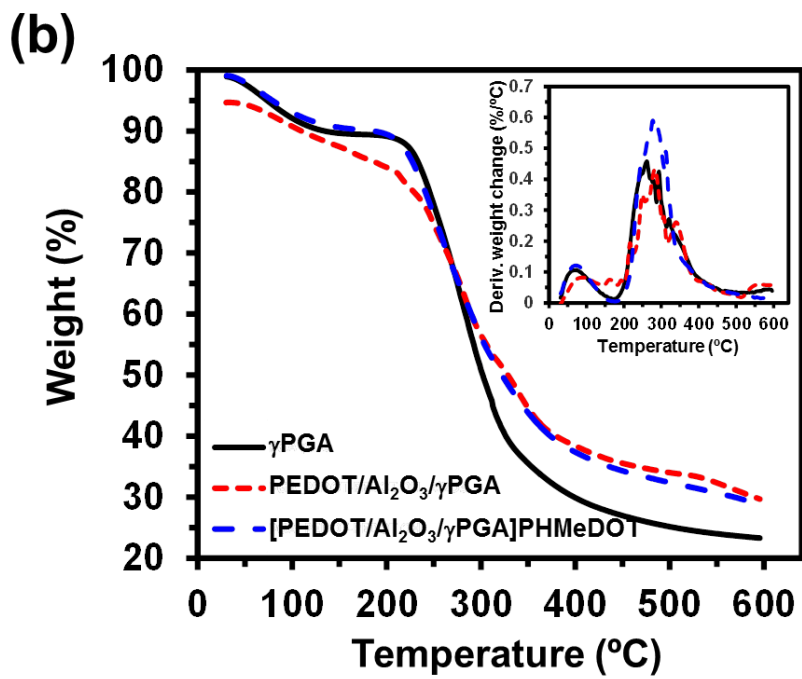
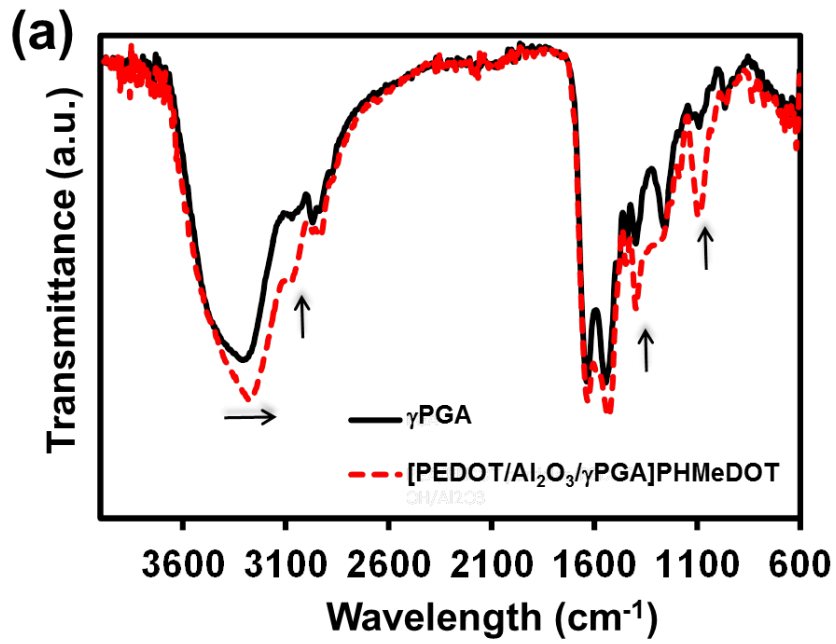


Figure 3

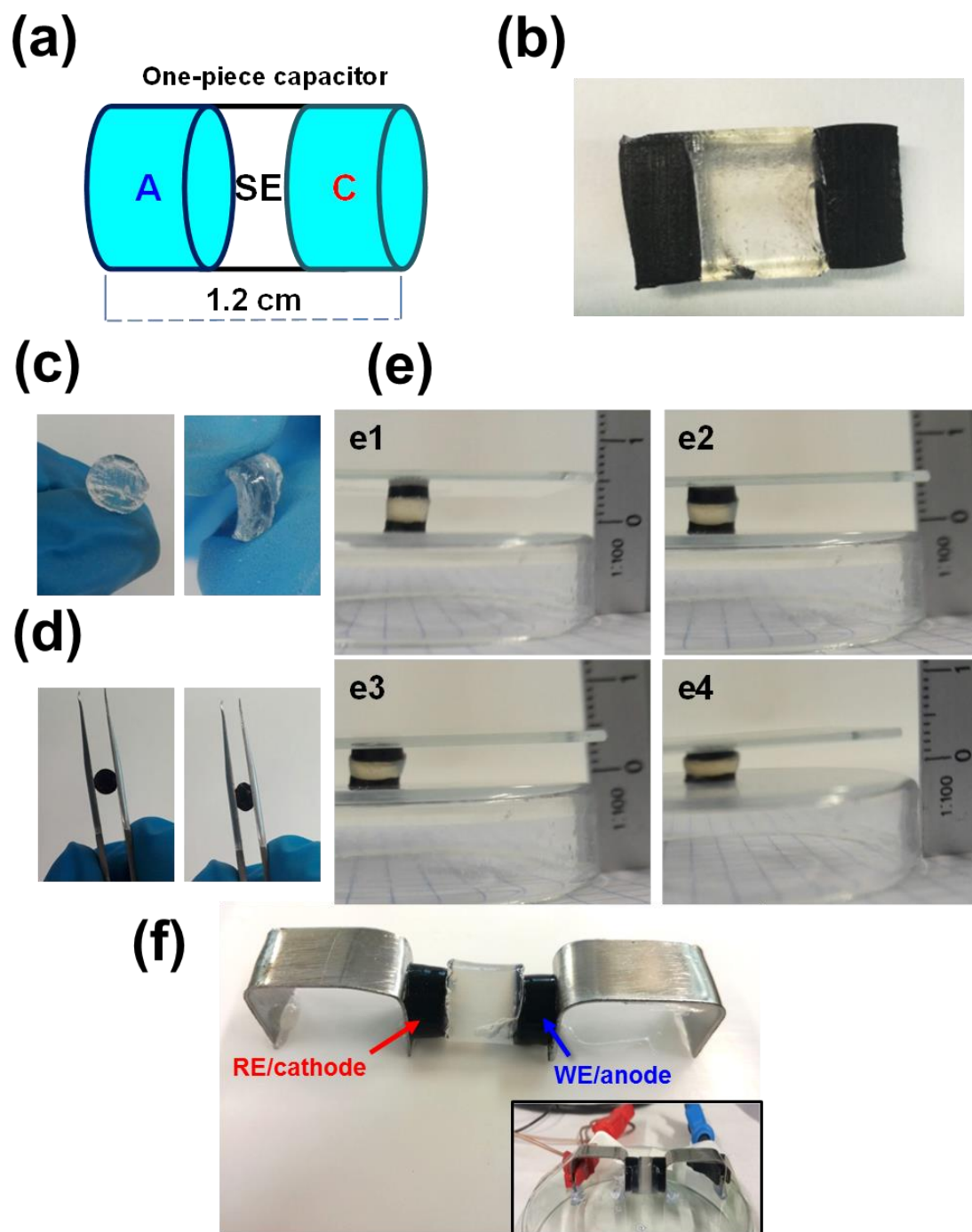


Figure 4

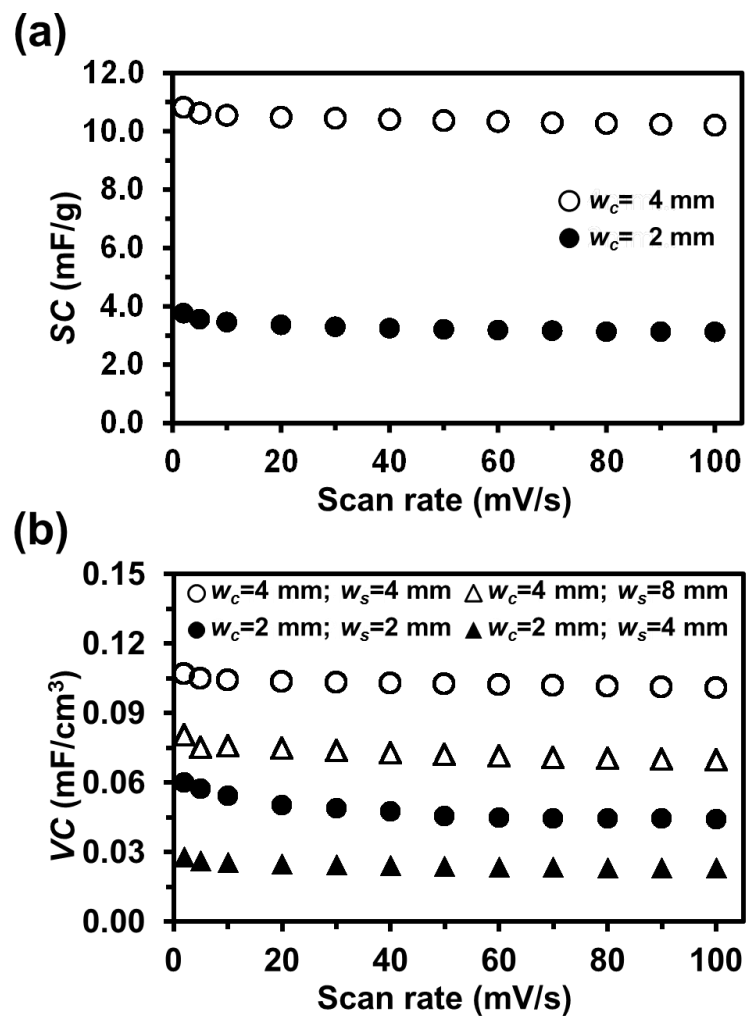


Figure 5

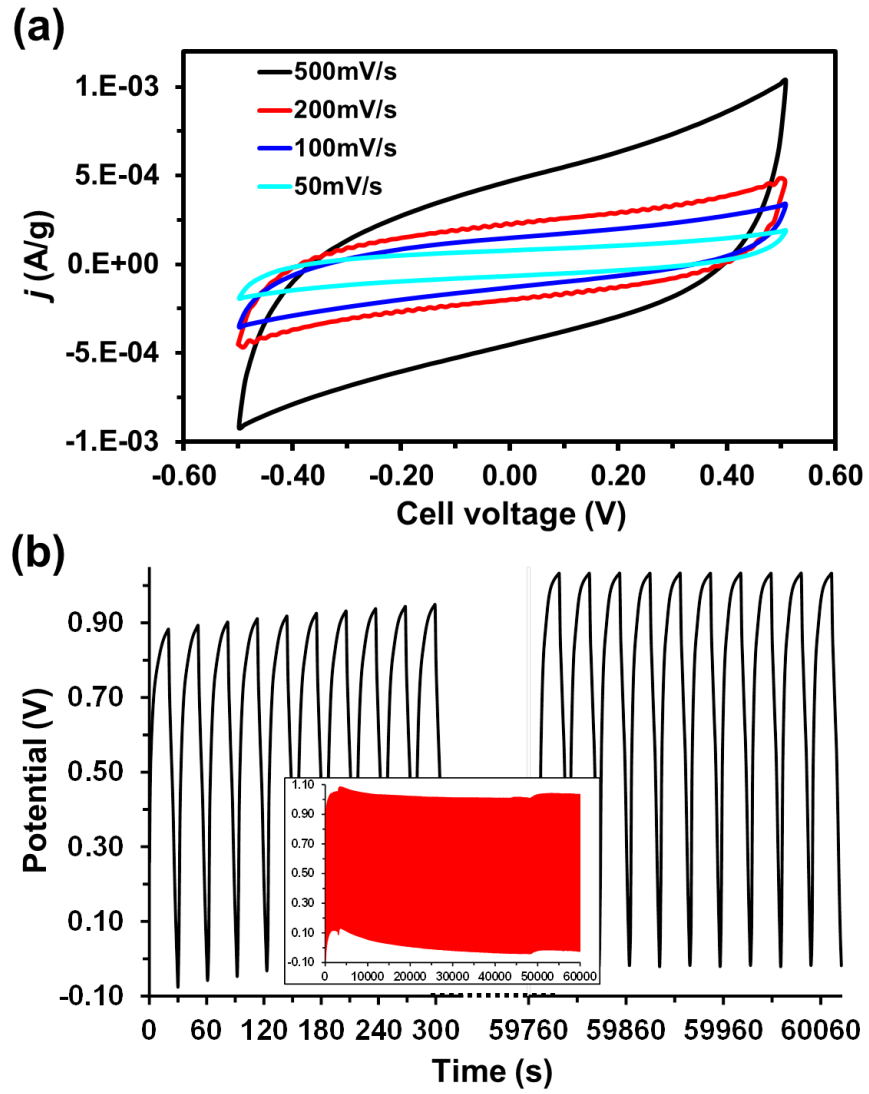


Figure 6

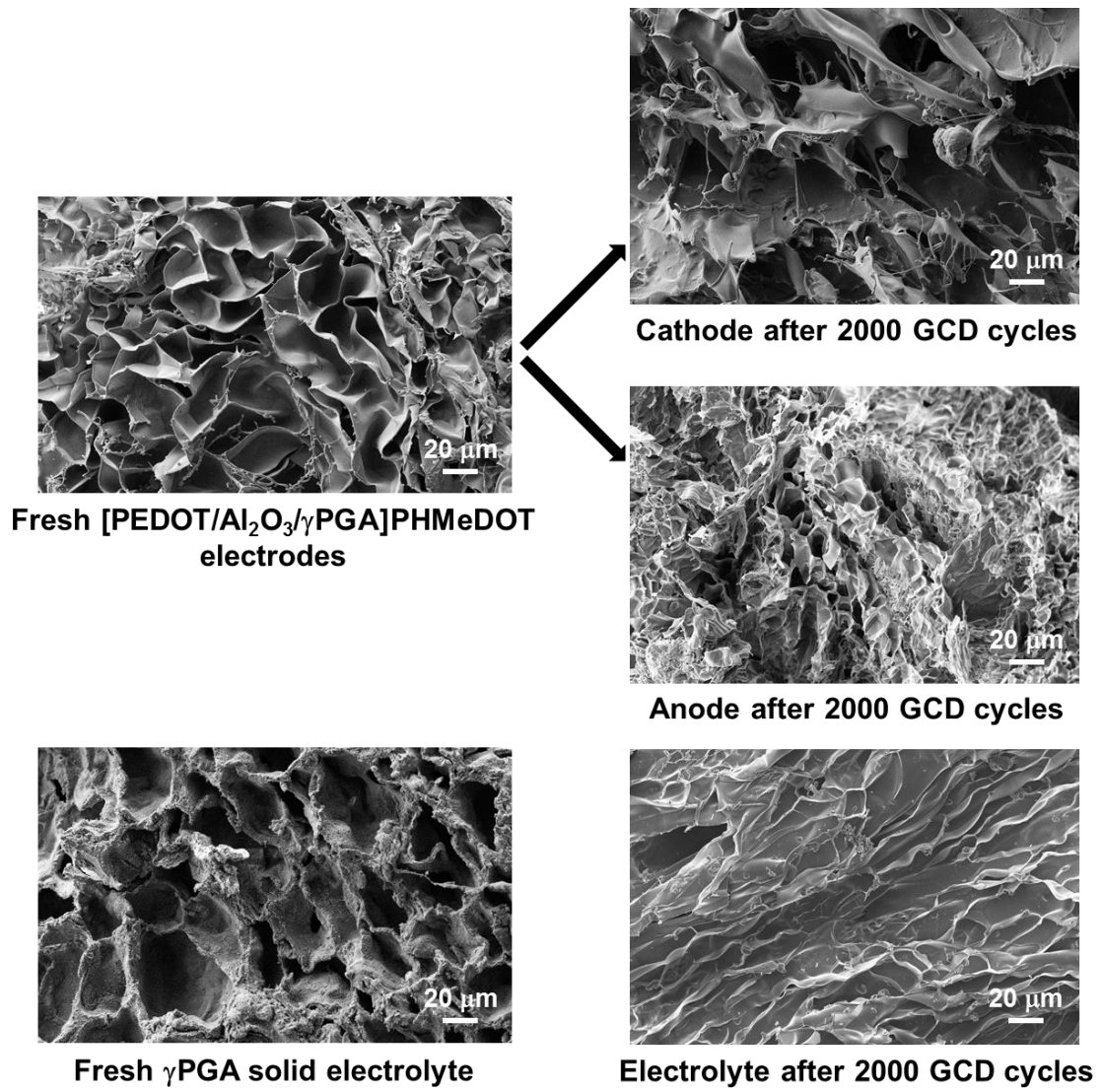


Figure 7

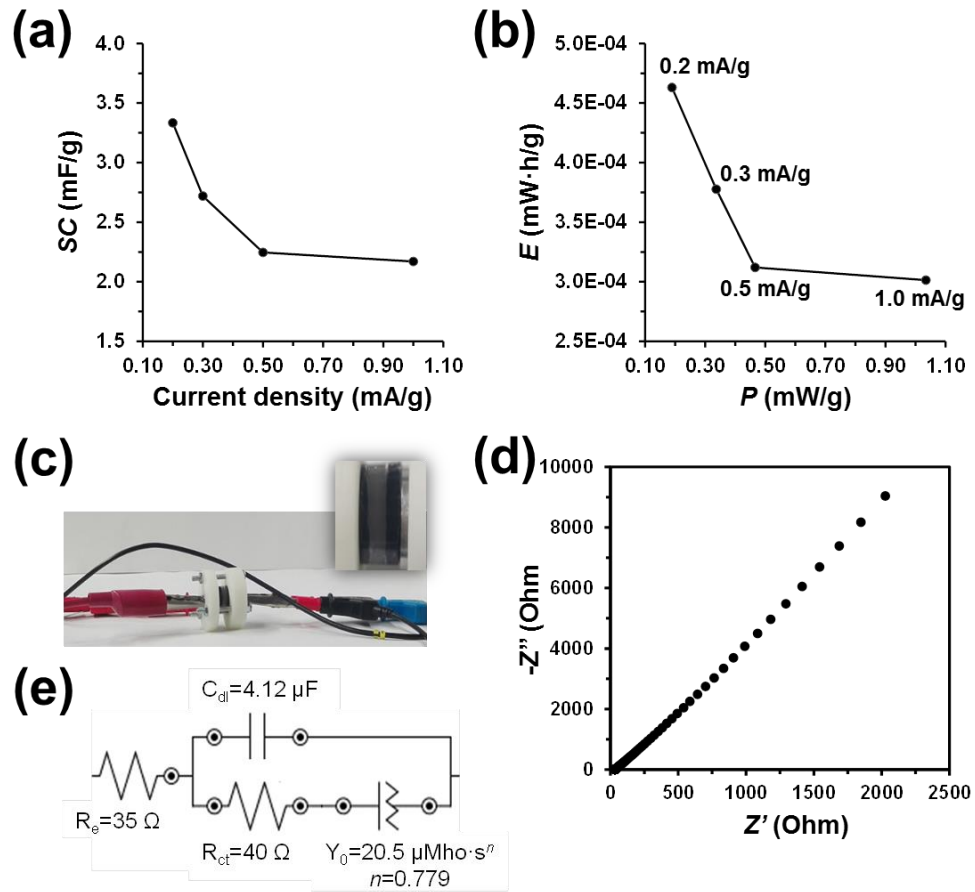


Figure 8

# GRAPHICAL ABSTRACT

